View metadata, citation and similar papers at core.ac.uk
brought to you by CORE
provided by Digital.CSIC

Correspondence

Beam Steering with Segmented Annular Arrays

Luis G. Ullate, Gregorio Godoy, Oscar Martínez, and Teresa Sánchez

***Abstract*—Two-dimensional (2-D) arrays of squared matrix have maximum periodicity in their main directions; consequently, they require half wavelength ($\lambda/2$), interelement spacing to avoid grating lobes. This condition gives rise to well-known problems derived from the huge number of array elements and from their small size. In contrast, 2-D arrays with curvilinear configuration produce lower grating lobes and, therefore, allow the element size to be increased beyond $\lambda/2$. Using larger elements, these arrays have the advantage of reducing the number of elements and of increasing the signal-to-noise ratio (SNR).**

In this paper, the beamforming properties of segmented annular phased arrays are theoretically analyzed and compared with the equivalent squared matrix array. In the first part, point-like elements are considered in order to facilitate the field analysis with respect to the array structure. Afterward, the effect of the element size on the steered beam properties also is presented.

In the examples, it is shown that the segmented annular array has notably lower grating lobes than the equivalent squared matrix array and that it is possible to design segmented annular arrays with interelement distance higher than λ whose beam characteristics are perfectly valid for volumetric imaging applications.

I. Introduction

Two-dimensional (2-D) arrays are useful for ultrasonic volumetric imaging because they produce steered and focused beams throughout a volume of interest. Typical 2-D arrays are based on a squared matrix (SM) configuration in which the array elements are the cells of the matrix. Due to the aperture periodicity, phased arrays require $\lambda/2$ spacing between elements in order to avoid unwanted grating lobes [1]. This condition gives rise to severe problems derived from the huge number of array elements, which becomes excessive in relation to the number of channels managed by current imaging systems, and from their small size, which causes a reduction in the signal-to-noise ratio (SNR).

Several techniques have been proposed in the literature to reduce the number of active array elements in SM arrays. One approach destroys the array periodicity by randomly removing a subset of elements from the full aperture [1]–[4]. Several methods for optimizing aperiodic layouts also have been proposed [5]–[7]. An alternative approach uses different arrangements of sparse periodic layouts for transmit and receive modes in which the grating lobes of the transmit array are suppressed by zeroes of the receive array response and vice versa. In this group can be included the cross-like configuration [8] and Vernier arrays [9], [10], which configure the transmission and reception apertures based on the Vernier scale. The concept of Vernier arrays was further extended to new 2-D layouts by exploiting either an increased number of symmetry axes or radial symmetry [11].

A constant of all these methods is that they maintain the $\lambda/2$ interelement spacing; thus, although they can produce beams of good properties, important problems relating to the SNR still remain, owing to the small size of the elements and the drastic reduction in the array active area.

As an alternative to these limitations, array apertures with curvilinear deployment have been proposed as they outperform rectilinear designs [12]–[15]. Due to their greater aperture spatial diversity, curvilinear arrays produce lower grating lobes and, therefore, layouts with interelement distance beyond $\lambda/2$ can be considered. In this sense, curvilinear arrays have the advantage of reducing the number of elements and, in addition, of enlarging the element size, thereby increasing the SNR associated with the element impedance and the array active area.

Our interest in this paper is to analyze theoretically the capability of segmented annular (SA) phased arrays for 3-D beamforming. A segmented annular array is a curvilinear array composed of a set of concentric rings of similar width that are divided into sectors. Although it is possible to configure this aperture in several ways, we consider only the case of elements with a similar area and unitary aspect ratio (Fig. 1), because, with these conditions, the beam properties are nearly optimized [14]. Computing methods for SA arrays based on the well-known spatial impulse response approach [16] are presented in [17], [18]. A theoretical description of the beam radiated by a single segmented annulus can be found in [19], [20]. Several simulations showing advantages of SA arrays in relation to SM arrays also have been presented, but the analysis is limited to particular cases, such as continuous wave [21] or unsteering [22]. Different layouts of SA arrays have been proposed for medical [23]–[25] and non-destructive testing [26], [27] applications.

In this work, the beamforming properties for equivalent SA and SM arrays are compared (two equivalent arrays have similar shape, size, active area, number of elements, and aspect ratio). In a first step, the analysis is made on the basis of the array factor (AF) function [28], which can

Manuscript received September 20, 2005; accepted May 10, 2006. This paper received the support of the Education and Science Ministry of Spain under its DPI2002-01583, DPI2004-06470, and DPI2004-06756 projects.

L. G. Ullate, O. Martínez, and T. Sánchez are with the Instituto de Automática Industrial (CSIC), La Poveda - 28500 Arganda del Rey, Madrid, Spain (e-mail: luisg@iai.csic.es).

G. Godoy is with the Departamento de Ingeniería Electrónica, de Telecomunicación y Automática, Universidad de Jaén, Linares, Jaén, Spain.

Digital Object Identifier 10.1109/TUFFC.2006.127

0885–3010/$20.00 © 2006 IEEE

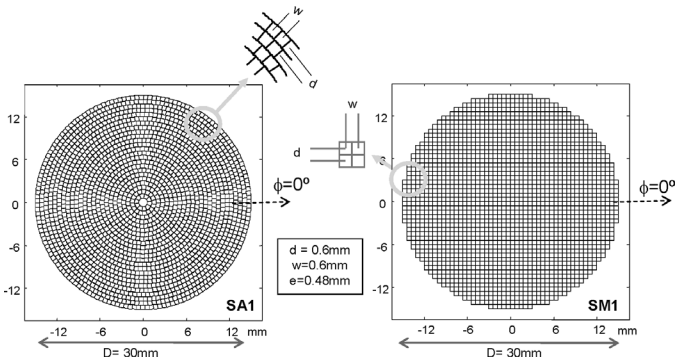

Fig. 1. Geometry of the equivalent arrays SA1 (left) and SM1 (right) with $D = 30$ mm, $d = w = 0.6$ mm, and $N = 1950$ elements of unitary aspect ratio with $e = 0.48$ mm of size.

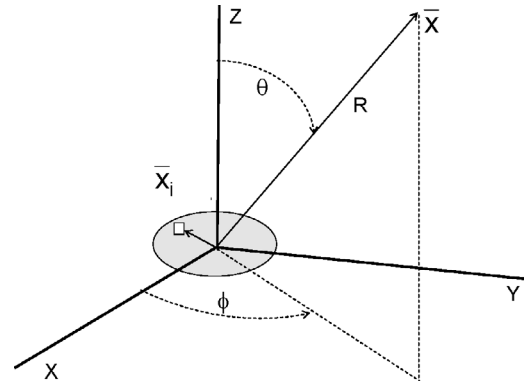

Fig. 2. Geometry of the coordinates system.

be obtained by replacing the actual elements with point sources vibrating in continuous wave (CW); this function facilitates the analysis of the beam properties in relation to the array structure. In a second step, the analysis is extended to wide-band excitation conditions. Steered-beam properties also are studied considering the real size of elements for both array configurations. Only the cases of full aperture and no apodization are considered in this work.

Fig. 1 shows the geometry of the two equivalent arrays on which the comparative analysis is based: a squared matrix array (SM1) and a segmented annular array (SA1) both of circular area with diameter $D = 30$ mm, containing $N = 1950$ elements of unitary aspect ratio. For both arrays, the interelement spacing is $d = w = 0.6$ mm and the element size is $e = 0.8$ d. Simulations are made considering that the arrays emit waves at 3 MHz into water, giving a wavelength of $\lambda \approx 0.5$ mm, and the array dimensions become $D = 60\ \lambda$ and $d = w \approx 1.2\ \lambda$ and $e \approx 0.96\ \lambda$. The analysis in wide band considers an ultrasonic pulse with a Gaussian envelope of 3 MHz central frequency and $B = 70\%$ relative bandwidth at -6 dB cut-off.

II. Computational Method

For simulations we assume a 2-D array of diameter D lying in the $Z = 0$ plane of a Cartesian coordinates system (Fig. 2). The N elements of the array vibrate in a pistonlike manner with velocity $v(t)$. The array emits ultrasonic waves, which propagate with velocity c through a homogeneous liquid medium of density ρ_0. Infinitely rigid baffle is assumed for boundary conditions. The pressure waveform $p(\cdot)$ radiated over a field point $\bar{x}$ is obtained by superposition:

$$p(\bar{x},t) = \rho_0 \frac{dv(t)}{dt} * \sum_{i=1}^{N} h_1\left(\bar{x}, t - T_i^F\right) = \rho_0 \frac{dv(t)}{dt} * h_A(\bar{x},t), \tag{1}$$

where $h_A(\cdot)$ is the velocity potential impulse response of the array, $h_i(\cdot)$ is the impulse response of the ith array element located at $\bar{x}_i$, $(*)$ indicates temporal convolution, and T_i^F are the time delays for focusing the beam at the point $\bar{x}^F$:

$$cT_i^F = \left|\bar{x}^F - \bar{x}_i\right| - \left|\bar{x}^F\right|. \tag{2}$$

The transmit-receive mode is simulated considering that the received signal $s(t)$ due to a point target at $\bar{x}$ is given by:

$$s(\bar{x},t) = \frac{\rho_0}{c}\frac{\partial^2 v(t)}{\partial t^2} * \left\{h_A^T(\bar{x},t) * h_A^R(\bar{x},t)\right\}, \tag{3}$$

where $h_A^T(\cdot)$ and $h_A^R(\cdot)$ are the emit and receive spatial impulse responses of the array.

The impulse response of the array elements can be calculated in the time domain by direct computation, dividing the array into squared cells of elementary area [29]. If the surface of the ith element is separated into N_i squared cells of elementary area ΔS, the velocity potential impulse response becomes the sum:

$$h_i^*(\bar{x},t) = \sum_{j=1}^{N_i} \frac{\delta\left(t - r_j/c\right)}{2\pi r_j}\Delta S, \tag{4}$$

where r_j is the distance from the jth cell to the field point $\bar{x}$, and h_i^* means the discrete representation of the impulse response.

In computations, the elementary cells are taken $\lambda/9 * \lambda/9$ of size and the sampling time is $\Delta t = \lambda/50c$. The computation error in these conditions is below 2% for every point in the field of interest [30].

When the array elements are assumed as point sources, the ultrasonic field is calculated from (3) and (4), considering single cells at the center of the array elements, with weight equal to the element area.

III. Array Factor Function

If we consider a linear array of identical elements, it is known that, in CW conditions, the pulse-echo response in the far field approximates to the field of a single element positioned at the origin (element factor) multiplied by a factor that is widely referred to as the AF [28]. Because

the AF does not depend on the directional characteristics of the radiating elements themselves, it can be simulated by replacing the actual elements with isotropic point-like sources. Each array has its own AF, which is a function of the geometrical layout, the steering angle and the pulse wavelength.

The pulse-echo analysis of 2-D arrays can be simplified by applying the projection-slice theorem [12], [31] and the effective aperture concept [9], [10]. The projection-slice method considers that the CW response of a 2-D array at a given azimuth direction ϕ can be found by projecting the 2-D element distribution on a line oriented at the ϕ direction (both 1-D and 2-D arrays are equivalent). However, the effective aperture of a linear array is the one-way aperture that has the same response as the pulse-echo response. In CW conditions, the effective aperture can be obtained from the spatial convolution of transmission and reception apertures. In this way, for every azimuth angle, the aperture of a 2-D array can be simplified to the aperture of a linear array, which is the convolution of the equivalent transmit and receive linear arrays at that direction. The elements' distribution on the effective aperture of the equivalent linear array is a determinant factor for the ultrasonic field in the side lobe region.

In the SM array case, the elements overlap for the main directions ($\phi = 0°$ and $90°$), resulting in a periodic equivalent linear array with $N_L = D/d$ weighted elements, all separated by a distance of d. The grating lobes in this case show peaks of amplitude similar to that of the main beam, whose angular position θ_G is [1]:

$$\theta_G \approx -\arcsin\left(\lambda/d - \sin\theta^F\right), \tag{5}$$

where θ^F is the beam steering angle. For $\phi = 45°$ and $135°$, the equivalent linear array also is periodic, but in this case the interelement distance is reduced to 0.7 d.

In contrast, SA arrays do not reach the periodicity of SM arrays. If we consider the equivalent linear array of a single annulus of radius R_k, ($R_k \gg d$, Fig. 3), the interelement distance d_i between two consecutive elements, which are located at the angular position ϕ_i with respect to the field point azimuth ϕ, can be approximated to:

$$d_i \approx d \sin\phi_i. \tag{6}$$

Therefore, the equivalent linear array of a ring is nonuniform, with interelement distance close to d at its center ($\phi_i \approx 90°$) and tending to zero at the extremes. By randomly rotating the array rings, the aperture spatial diversity of the SA array can be optimized.

From these arguments, the AF beam patterns of Fig. 4 can be explained. SM1 generates at the main directions ($\phi = 0°$ and $\phi = 90°$) grating lobes of the same amplitude as that of the main lobe, which, in agreement with (5), are located at $\theta_G \approx \pm 56°$ [Fig. 4(c)]. A comparison of SM1 and SA1 AF gives the following results:

- Because the main beam is mainly determined by the global aperture, both arrays produce practically identical main lobes, which also are coincident with the equivalent circular aperture. The pulse-echo beam widths at −6 dB, −20 dB, and −50 dB are given in Table I.
- However, the two arrays, however, have significant differences in the side-lobe region. SA1 grating lobes spread almost uniformly on a ring around the main lobe, with −37 dB peak level. As the remaining periodicity of SA1 is mostly determined by the interelement distance d, the grating-lobe peak angular position also is given by (5).
- We can define the concept of directional periodicity $P(\phi)$of a 2-D array as the ratio between the peak of secondary lobes of the equivalent linear array at a given direction ϕ ($SL_{\text{Peak}}(\phi)$) and the main-lobe peak (ML_{Peak}), both calculated from the array factor function:

$$P(\phi) = \frac{SL_{\text{Peak}}(\phi)}{ML_{\text{Peak}}}. \tag{7}$$

This parameter is useful because, being only a function of the array layout and the acoustic wavelength, it allows a quick estimation of the influence of the array structure on the generation of secondary lobes. Fig. 4(d) is a logarithmic representation of this concept; it shows the ratio between the main lobe and the peaks of the side-lobe region (given by $|\theta| > 8°$) in relation to the azimuth angle ϕ. Although SM1 produces a nonregular directional periodicity showing peaks of secondary lobes with maximum amplitude at the array main directions, SA1 produces an annular pedestal with small variations of the directional periodicity ranging from −37 dB to −50 dB and a mean value for all ϕ of −47 dB.

The array global periodicity $P_{\max}$ also can be defined as the ratio between the maximum value of the side-lobe region (SL_{Peak}) and the main lobe:

$$P_{\max} = \max_{\phi=0.180°}(P(\phi)) = \frac{SL_{\text{Peak}}}{ML_{\text{Peak}}}. \tag{8}$$

Fig. 4(d) shows that SM1 has maximum global periodicity ($P_{\max}(SM1) = 1$) and $P_{\max}(SA1) \approx 0.01$,

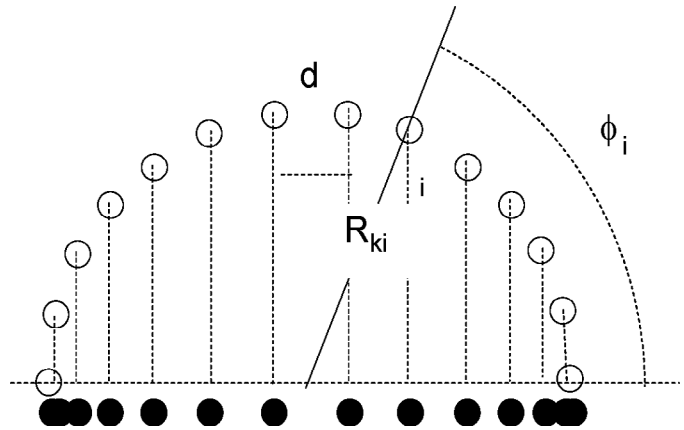

Fig. 3. Equivalent linear array of the kth segmented annulus.

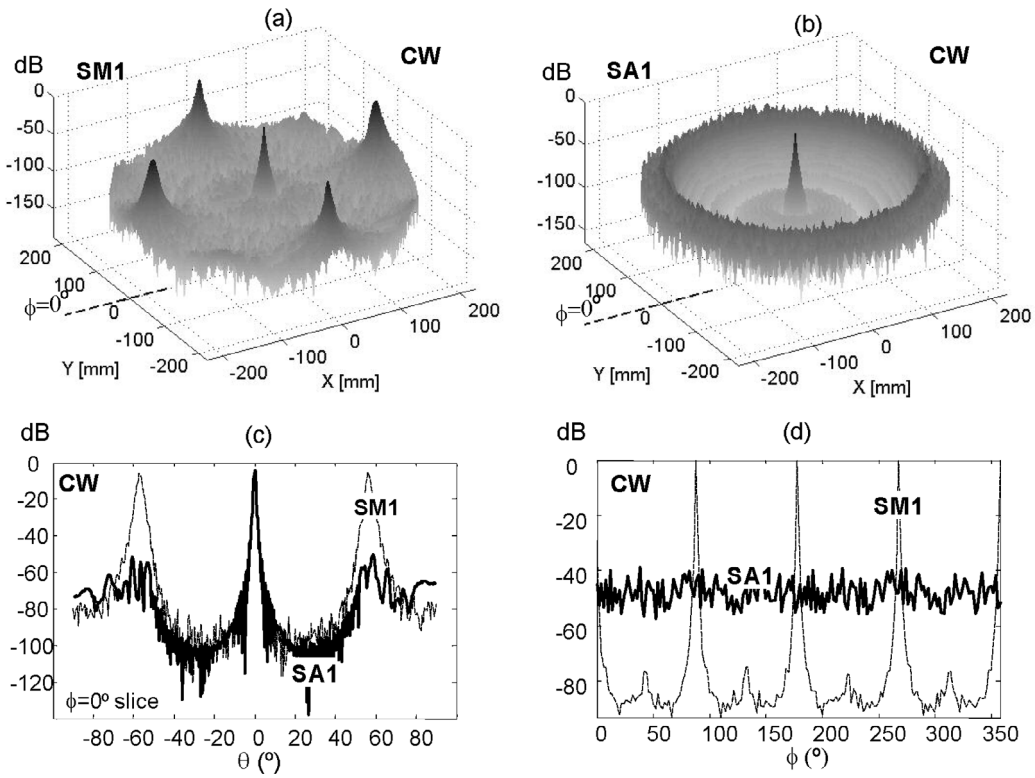

Fig. 4. Array factor of SM1 and SA1 (the array factor considers that the array elements are points vibrating in a continuous wave). (a) and (b), 3-D representation of SM1 and SA1 beam patterns in pulse-echo mode focusing at $R^F = 225$ mm on axis. (c) Continuous wave beam pattern (two-ways) at the azimuth direction $\phi = 0°$. (d) Peak value of the side-lobe region ($|\theta| > 8°$) for every slice, as a function of the azimuth angle ϕ.

TABLE I

BEAM PROPERTIES CONSIDERING THAT SM1 AND SA1 ARRAYS ARE FORMED BY POINT SOURCES EMITTING IN CW AND WB.[1]

		Main-lobe region			Side-lobe region	
		$\Delta\alpha(-$ dB)	$\Delta\alpha(-20$ dB)	$\Delta\alpha(-50$ dB)	SL_{Peak}	SL_{Average}
CW	SM1	0.96°	1.65°	5.45°	0 dB	−60 dB
	SA1	0.95°	1.64°	5.38°	−37 dB	−64 dB
WB	SM1	0.89°	1.64°	4.66°	−32 dB	−69 dB
	SA1	0.89°	1.63°	4.63°	−59 dB	−72 dB

[1] $\Delta\alpha$ is the main-lobe beamwidth in degrees at different levels. SL_{Peak} is the ratio between the peaks of the side-lobe ($|\theta| > 8°$) and the main-lobe regions. SL_{Average} is the ratio between the mean value of the field amplitude at the side-lobe region and the main-lobe peak. All values are for the unsteering transmission-reception case.

indicating a reduction of two orders of magnitude in the peak of secondary lobes in favor of SA1 for the pulse-echo case.

- The mean value at the side-lobe region SL_{Average} has also been considered in the comparisons, because this parameter is useful for optimizing array designs. Table I shows that SL_{Average} is −60 dB and −64 dB for SM1 and SA1, respectively.
- The variations of the function $P(\phi)$ in SA arrays [Fig. 4(d)] are mainly due to particular periodicities between rings appearing in the equivalent linear array at certain directions, which can also affect the peak of the side-lobe region. In order to evaluate the influence of the array layout on the array response, 13 SA arrays have been designed by randomly rotating their rings. Comparing their field properties, it has been observed that the main beams and the mean level of the side-lobe region are very similar for the 13 apertures. But the peak value of this region varies from −39 dB to −33 dB, depending on the particular layout (Fig. 5). This means that, when designing SA arrays, it is worth trying out several designs in order to find the layout with the lowest SL_{Peak}.

IV. Omni-Directional Elements Vibrating in Wide-Band Pulses

In this section, the comparative analysis is made by considering that the arrays are formed by ideal point-like

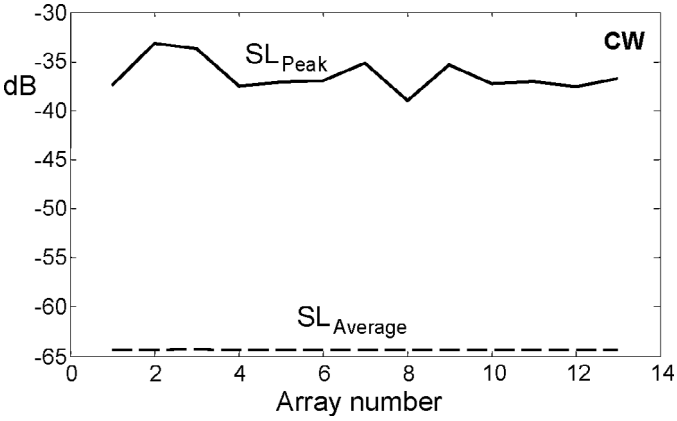

Fig. 5. Array factor. Level of secondary lobes for 13 arrays equivalent to SA1 (considering point-like transducers), which have been designed by randomly rotating the array rings. SL_{Peak}. Peak value of the side-lobe region ($|\theta| > 8°$). SL_{Average}, mean value of the side-lobe region.

transducers emitting wide-band (WB) pulses. Fig. 6 shows the field in WB conditions, about which we can make the following comments:

- The main beams of SM1 and SA1 are very similar as they are mainly determined by the aperture geometry; the quantitative values for CW and WB conditions can be observed in Table I. However, as occurred with the AF, the structure of secondary lobes is very different for the two arrays. SM1 produces grating lobes concentrated in specific azimuth directions giving a double-cross aspect to the field. SA1 generates grating lobes that spread almost uniformly along a wide ring centered on the main lobe. Norton [32] has described for the linear array and for several pulse envelops (e.g., rectangular or Gaussian) the effect of the pulse bandwidth on the grating lobe amplitude, which is affected by a bandwidth factor F_{WB} that increases with the number of cycles of the ultrasonic pulse n_c:

$$SL_{\text{Peak}}^{SM} = F_{\text{WB}} \approx \frac{n_c}{N_L} \approx \frac{k \cdot d}{BD}, \tag{9}$$

  where N_L indicates the number of elements of the linear array, B is the pulse relative bandwidth that is inversely proportional to n_c, and k is a factor close to one that depends on the pulse shape. Considering a linear array with $D/d = 50$ emitting a pulse with $B = 0.7$ at -6 dB cut-off, we found $k = 0.84$.
  We can translate the same method to the main directions of the squared matrix array. Using the previous values of B and k in (9) gives $F_{\text{WB}} = -32$ dB for SL_{Peak}, which is almost the computed value shown in Table I for SM1.
  In the case of segmented annular apertures, SL_{Peak} is affected by two factors: the bandwidth factor and the array global periodicity in WB P_{WB}^{SA}, which, due to the limited number of pulse cycles, is not coincident with the CW periodicity. The array global periodicity in WB is then a complex function of the array structure and the pulse bandwidth, which determines the array portion causing cancellation in the grating lobes:

$$SL_{\text{Peak}}^{SA} \approx F_{\text{WB}} \cdot P_{\text{WB}}^{SA}(B). \tag{10}$$

  In order to facilitate the analysis, we consider that F_{WB} is similar to the one computed for the equivalent SM array: -32 dB (making this approximation, for the intervals $0.2 \leq B \leq 0.7$ and $20 \leq D/d \leq 50$ we have computed errors within ± 3 dB). In the SA1 case and taking a pulse bandwidth $B = 0.7$, the array global periodicity can be determined from (10) and the peak of the side-lobe region given in Table I (-59 dB), giving for P_{WB}^{SA} a value of -27 dB; this means that, compared to CW, the WB ($B = 0.7$) produces a reduction of 10 dB in the grating lobe cancellation.
  Due to the WB, grating lobes spread over a broader region of the space, starting at $|\theta| \approx 30°$ for both arrays [Fig. 6(c)]. Moreover, due to the higher frequency components of the ultrasonic pulse, the grating lobes at the array diagonals of SM1 increase in relation to CW [Fig. 6(d)].
- The influence of the parameter d/λ on the side lobe region is shown in Fig. 7, which has been computed considering that SM1 and SA1 are formed by ideal point-like elements, and varying the central frequency of the WB pulses but holding the relative bandwidth at $B = 0.7$.
  Both arrays present very similar behavior with SL_{Peak} practically constant in all the range of d/λ (but holding a difference of 30 dB in favor of SA1), indicating that this parameter does not have much influence on the peak of the side-lobe region. The reduction observed in SL_{Peak} when $d/\lambda < 1$ is because we have computed the unsteered case, and the grating lobes are partially hidden in the back region of the transducer. SL_{Average} also is constant for both arrays when $d/\lambda > 1$ with a very small difference of 5 dB in favor of SA1. Fig. 7 also shows that the grating-lobe peak position is very similar for SM1 and SA1.
- The influence of the number of array elements N on the secondary lobes is shown in Fig. 8, which has been obtained by removing one by one the external rings from SA1. The variation of SL_{Peak} for the SM array is due to the bandwidth factor F_{WB}, which is a function of the array diameter D. The periodicity factor P_{WB} is given in decibels by the difference between SM and SA curves of Fig. 8, and it shows a variation from -12 dB to -30 dB for $100 < N < 1900$. This indicates that, in the case of the SA array, an important dependence of SL_{Peak} exists and, therefore, of the array global periodicity on the number of elements (approximately inverse to N in the two-ways case) in contrast with other array design parameters, which do not produce such strong variations. However, the curves of SL_{Average} are very similar for SM and SA arrays, meaning that this parameter is mainly determined by the number of elements, rather than by the array type. An inverse relation exists between N and

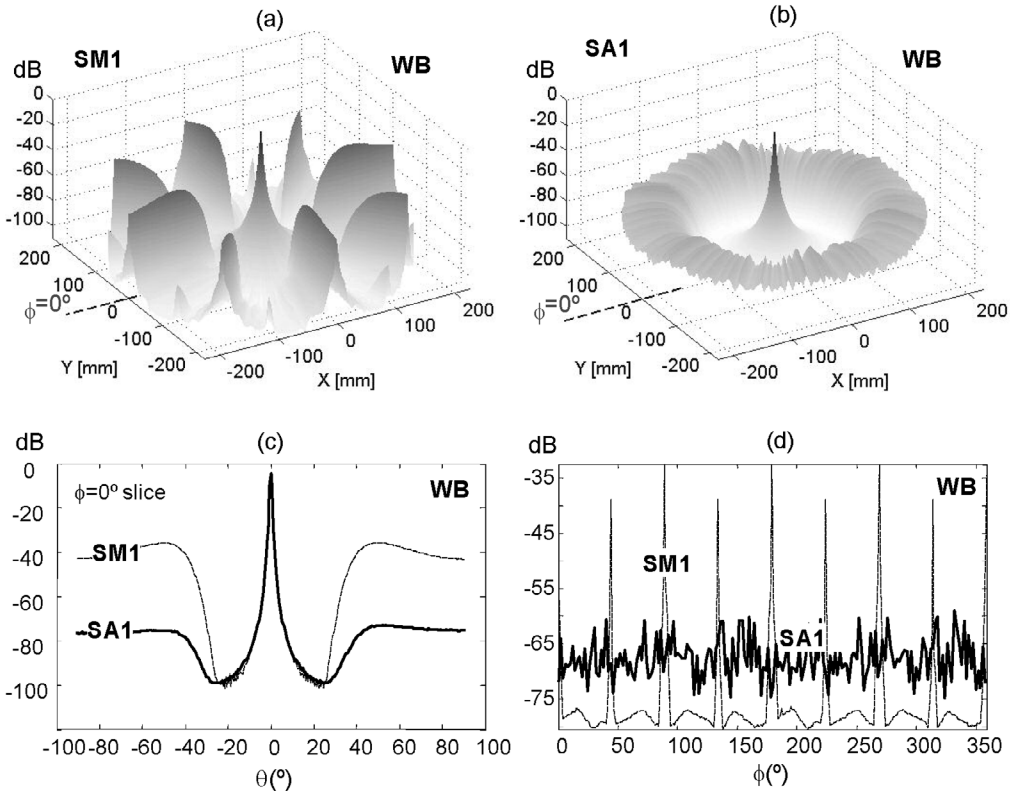

Fig. 6. (a) and (b), Pulse-echo beam pattern of SM1 and SA1 with ideal point-like elements vibrating in WB. (c) Lateral profiles at the azimuth direction $\phi = 0°$. (d) Peak value of the side-lobe region ($|\theta| > 8°$) for every slice, as a function of the azimuth angle ϕ.

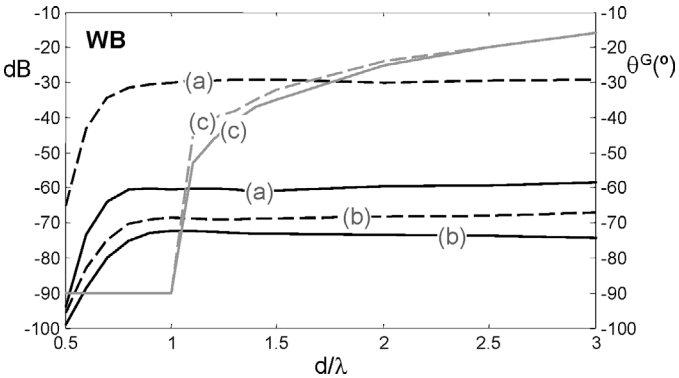

Fig. 7. Variations at the side-lobe region as a function of d/λ, considering that the array elements are ideal points vibrating in WB. (a) Peak value of the side-lobe region. (b) Mean value of the side-lobe region. (c) Angular position of SL_{Peak}. Dashed lines, SM1; solid lines, SA1.

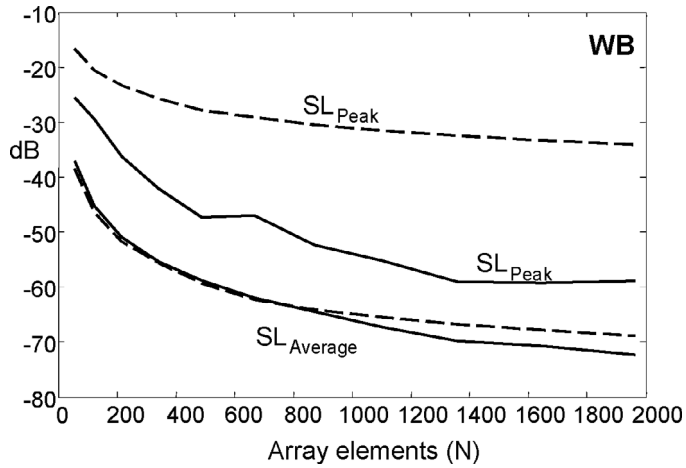

Fig. 8. Peak and average of the side lobe-region as a function of the number of array elements N, considering that the elements are ideal points vibrating in WB. Solid line, SA array. Dashed line, SM array. The interelement distance is maintained at $d = 1.2\ \lambda$.

SL_{Peak} or SL_{Average}, indicating that, when the number of elements is low, the side-lobe properties are not good enough for image applications. A low limit for the full array could be $N = 300$, which gives SL_{Peak} below -40 dB and SL_{Average} at about -55 dB.

V. Effect of Real Size of Array Elements

We have shown that the aperture spatial diversity inherent in SA arrays produces lower grating lobes, allowing the interelement distance to be increased beyond $\lambda/2$, typical restriction of SM arrays. In this section, the beam properties of SM1 and SA1 are analyzed considering that the element size is finite with $e = 0.8$ d.

A. CW Beam Properties

Fig. 9 shows the CW beam pattern of SM1 and SA1 in the focal semisphere, focusing at ($R^F = D^2/8\lambda$, $\phi^F =$

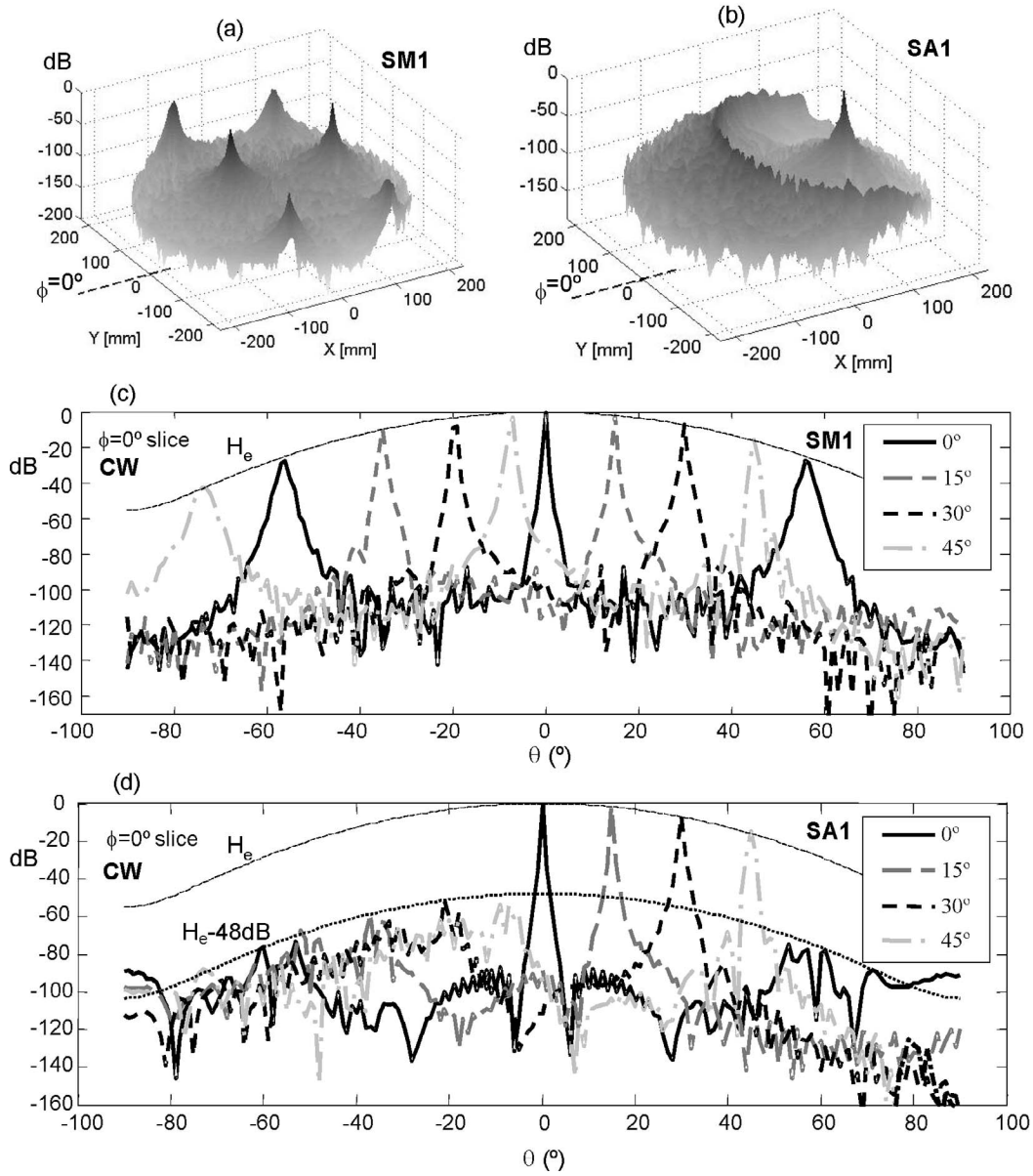

Fig. 9. CW beam patterns of SM1 (a)–(c) and SA1 (b)–(d) considering the real size of elements ($e = 0.8$ d). (a) and (b), 3-D representation of the focal semisphere in pulse-echo focusing at $R^F = D^2/8\lambda$, $\phi^F = 0°$, $\theta^F = 30°$. (c) and (d), $\phi = 0°$ slice for the following values of steering angle, $\theta^F = 0°$, 15°, 30°, and 45°.

0°, $\theta^F = 30°$). It is well-known [1] that the field in the focal semisphere of a SM array can be approximated to the product of an element factor $H_e(\theta, \phi)$ and the array factor function $AF(\theta, \phi)$. The element factor in pulse-echo is just the square of the Fourier transform of the element aperture multiplied by an obliquity factor, which is constant given the infinitely rigid nature of the baffle assumed in this paper. For every slice ϕ, the array lateral response LR (this is the main lobe peak modulating curve) is given by:

$$LR(\phi, \theta) = H_e(\phi, \theta) \cdot AF(\phi, \theta), \tag{11}$$

where [2]:

$$H_e(\phi, \theta) \approx \sin c^2\left(\frac{e}{\lambda}\cos\phi\sin\theta\right)\sin c^2\left(\frac{e}{\lambda}\sin\phi\sin\theta\right). \tag{12a}$$

Making $\phi = 0°$ we obtain the worst field case for SM1:

$$LR(\phi = 0°, \theta) = H_e(\phi = 0°, \theta) \approx \sin c^2\left(\frac{e}{\lambda}\sin\theta\right). \tag{12b}$$

In the $\phi = 0$ slice, the lateral evolution of both the main-lobe and the grating-lobe peaks during steering is modulated by the element factor in this form:

$$ML \approx H_e(\phi = 0°, \theta^F), \tag{13}$$

$$SL_{\text{Peak}} \approx H_e(\phi = 0°, \theta^G), \tag{14a}$$

where θ^G is given in (5). The modulating effect of the element factor is clearly shown in Fig. 9(c) in which the

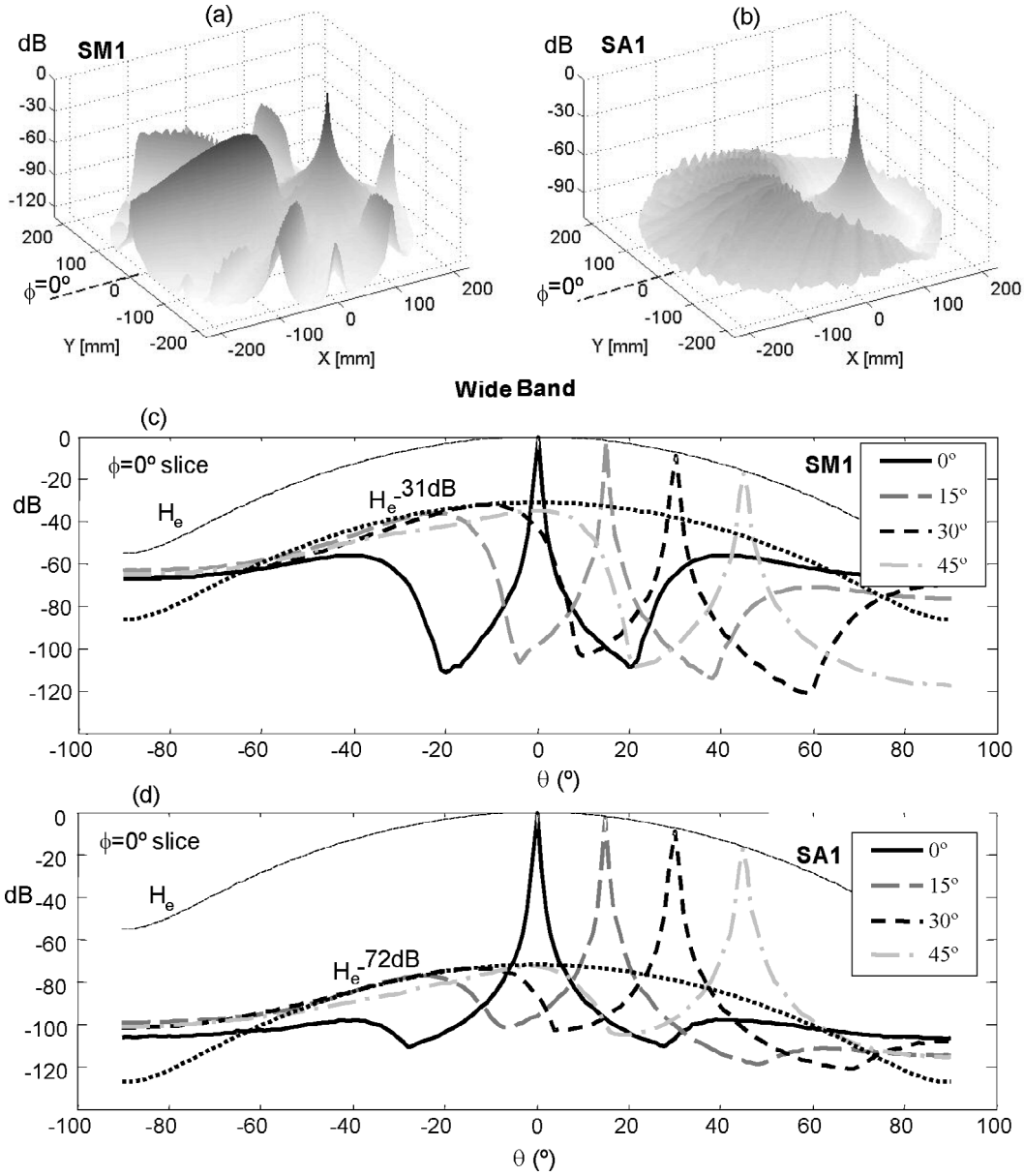

Fig. 10. WB beam patterns of SM1 (a)–(c) and SA1 (b)–(d) considering the real size of elements ($e = 0.8$ d). (a) and (b), 3-D representation of the focal semisphere in pulse-echo focusing at $R^F = D^2/8\lambda$, $\phi^F = 0°$, $\theta^F = 30°$. (c) and (d), $\phi = 0°$ slice for $\theta^F = 0°$, 15°, 30°, and 45°.

CW lateral responses of SM1 at different steering angles are drawn. It can be observed that the theoretical element factor $H_e(\theta)$ given in (12b) is nearly the envelope of both the main-lobe and the grating-lobe peaks.

The steered beam properties for the segmented annular array SA1 can be observed in Figs. 9(b) and (d)]. On the one hand, the main-lobe peak also is modulated by a curve $LR(\theta)$, which is independent of ϕ, whose value approximately integrates all the element factors $H_{e,SA}(\phi_i, \theta)$ with their particular azimuth orientations ϕ_i. There is not an expression for $H_{e,SA}(\phi, \theta)$. However, we can simplify the problem if we consider that, when the array elements are very small, the lateral response of a segmented annular element is very similar to the equivalent squared element given by (12a). The estimation of the array lateral response can be further simplified if we consider that (for small elements) within the scanning zone of interest ($-45° \leq \theta^F \leq 45°$), $H_e(\phi, \theta)$ is almost invariant with respect to ϕ, as the difference of amplitudes of $H_e(\phi, \theta)$ changing the azimuth orientation ϕ is in the range of ± 1 dB. Therefore, we can consider $H_{e,SA}(\phi, \theta) \approx H_{e,SA}(\theta) \approx H_{e,SM}(\phi = 0°, \theta)$ (12b), producing errors that are in the range of ± 1 dB for the scanning zone of interest ($-45° \leq \theta^F \leq 45°$). This effect can be observed in Fig. 9(d) in which the main lobe peak of the SA array is approximately modulated by the element factor $H_{e,SM}(\phi = 0°, \theta)$ of the equivalent SM array.

Besides the main lobe, the grating lobe ring (which is centered on the focus) also is affected by the element factor $H_{e,SA}(\theta)$, causing major reduction of amplitude to the points of major θ. Thus, the grating lobe peak will be given at the point of the grating lobe ring with maximum $H_e(\theta)$,

which is located in the $\phi = \phi^F$ slice at $\theta \approx \theta^F - \theta^G$. This is the section presented in Fig. 9(d) in which it can be observed that the grating lobes are modulated by the element factor $H_e(\theta)$ of (12b), but in this case with a drop of 48 dB with respect to the main lobe [this quantity agrees with the array periodicity at the $\theta = 0$ slice shown in Fig. 4(c)].

Therefore, for segmented annular arrays, the grating-lobe peak during steering can be written in a more generalized form than (14a):

$$SL_{\text{Peak}}\left(\phi^F\right) \approx P\left(\phi^F\right) \cdot H_e\left(\theta^F - \theta^G\right). \tag{14b}$$

As $P(\phi)$ has small variations in relation to the azimuth angle, this function can be replaced by a global periodicity factor taking either the average of $P(\phi)$ or its maximum $P_{\max}$ (8) for the worst ϕ case.

B. Beam Properties in Wide Band

Fig. 10 shows the WB beam patterns of SM1 and SA1 in the focal semisphere, focusing at ($R^F = D^2/8\lambda$, $\phi^F = 0°$, $\theta^F = 30°$). In this case, the lateral evolution of the main-lobe peak during steering is modulated by the element factor $H_e(\theta)$, and the grating-lobe peak evolution is affected by three factors: the element factor H_e, the WB factor, and the array periodicity in the WB P_{WB}:

$$SL_{\text{Peak}}\left(\phi^F\right) \approx F_{\text{WB}} \cdot H_e\left(\theta^F - \theta^G\right) \cdot P_{\text{WB}}\left(\phi^F\right). \tag{14c}$$

For SM1, the grating-lobe peak is produced in the main directions where $P_{\text{WB}} = 1$. The vertical distance between both H_e envelope curves of Fig. 10(c) is -31.5 dB, which is in agreement with the value of F_{WB} given in Table I. For SA1, the vertical distance between the envelope curves of Fig. 10(d) is -72 dB, which is in accordance with SL_{Peak} at the $\phi = 0°$ slice shown in Fig. 6(c).

The evolution of the main-lobe and the grating-lobe peaks in relation to the steering angle for SA1 can be observed in Fig. 11. It shows that, for SA1 in WB, it is possible to reach steering angles up to 40° with more than 50 dB of dynamic range and SL_{Average} of -64 dB. This result indicates that SA1 could be an adequate candidate for the generation of volumetric images, although it goes beyond the restrictions of typical 2-D arrays in relation to the interelement distance ($d = 1.2\ \lambda$) and the element size ($e \approx \lambda$).

We should underline that (14a) to (14c) have only a relative quantitative validity, being more useful for qualitative descriptive purposes. For instance, they can be applied for the analysis of Fig. 12, which shows, for small ($D = 20\ \lambda$) and large ($D = 60\ \lambda$) aperture sizes, a comparison of the dynamic range (ratio between the peaks of the side-lobe and the main-lobe regions) in relation to the interelement distance. The element size is $e = 0.8$ d and the array has been focused at ($R^F = D^2/8\lambda$, $\theta^F = 0°$, $\theta^F = 30°$) in all cases. We shall refer to SM-20 and SA-20 as the arrays with $D = 20\ \lambda$, and SM-60 and SA-60 as the arrays with $D = 60\ \lambda$.

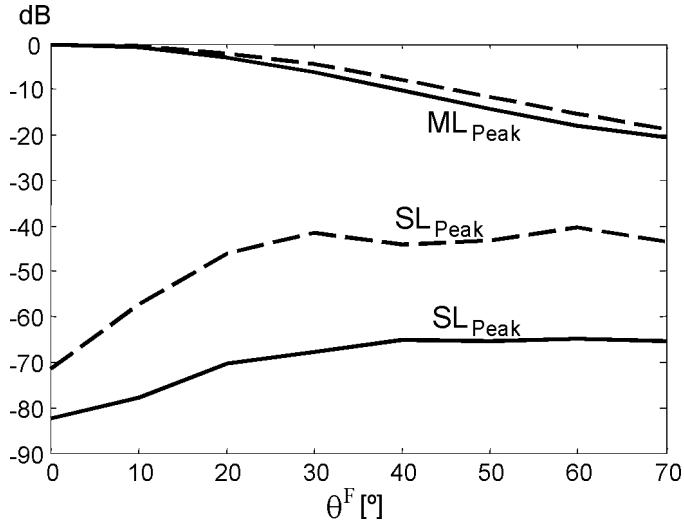

Fig. 11. SA1 array considering the real size of elements: evolution of the main-lobe peak (ML_{Peak}) and the peak of the side-lobe region (SL_{Peak}) as a function of the steering angle θ^F. Dashed line, CW excitation; solid line, WB pulse.

In CW conditions [Fig. 12(a)], the peak of the side-lobe region for the SM arrays does not change with the array size, showing a small variation around the 0 dB level for the interval $0.7 \leq d/\lambda \leq 1.5$, which is mainly due to the modulating effect of the element factor H_e. In the case of SA arrays, besides the smooth variation related to the element factor, SL_{Peak} shows an additional reduction associated with the smaller array periodicity, at levels of -24 dB and -37 dB for SA-20 and SM-60, respectively. In contrast, the side-lobe average [Fig. 12(b)] is not a function of the array type, and equivalent arrays have similar side-lobe average. However, it is a function of the number of array elements.

The curves corresponding to WB conditions are shown in Figs. 12(c) and (d). Due to the bandwidth factor F_{WB}, which depends on D and d (9), SL_{Peak} curves corresponding to the four array designs become separated, but they still remain nearly parallel. The step between SM-60 and SM-20 curves is -10 dB, which corresponds to the ratio between diameters. A -22 dB step is observed between the curves corresponding to the small arrays; this difference is -32 dB for the large arrays. The average of the side-lobe region does not present variations with either the array type (SM or SA) or the pulse bandwidth (CW or WB), as the array size and the number of elements are more decisive for this parameter. From these figures we can deduce that, within 30° of the steering angle, a SA array with $D = 60\ \lambda$ and $d = 1.2\ \lambda$ produces a side-lobe region with $SL_{\text{Peak}} = -53$ dB and $SL_{\text{Average}} = -82$ dB, which can be valid for ultrasonic imaging. In this case, the full aperture would be used, and the number of elements would be reduced from 11310 to 1950 (a factor of 5.8!) with respect to a SM array with $\lambda/2$ interelement spacing; the element area also would be multiplied by the same factor. However,

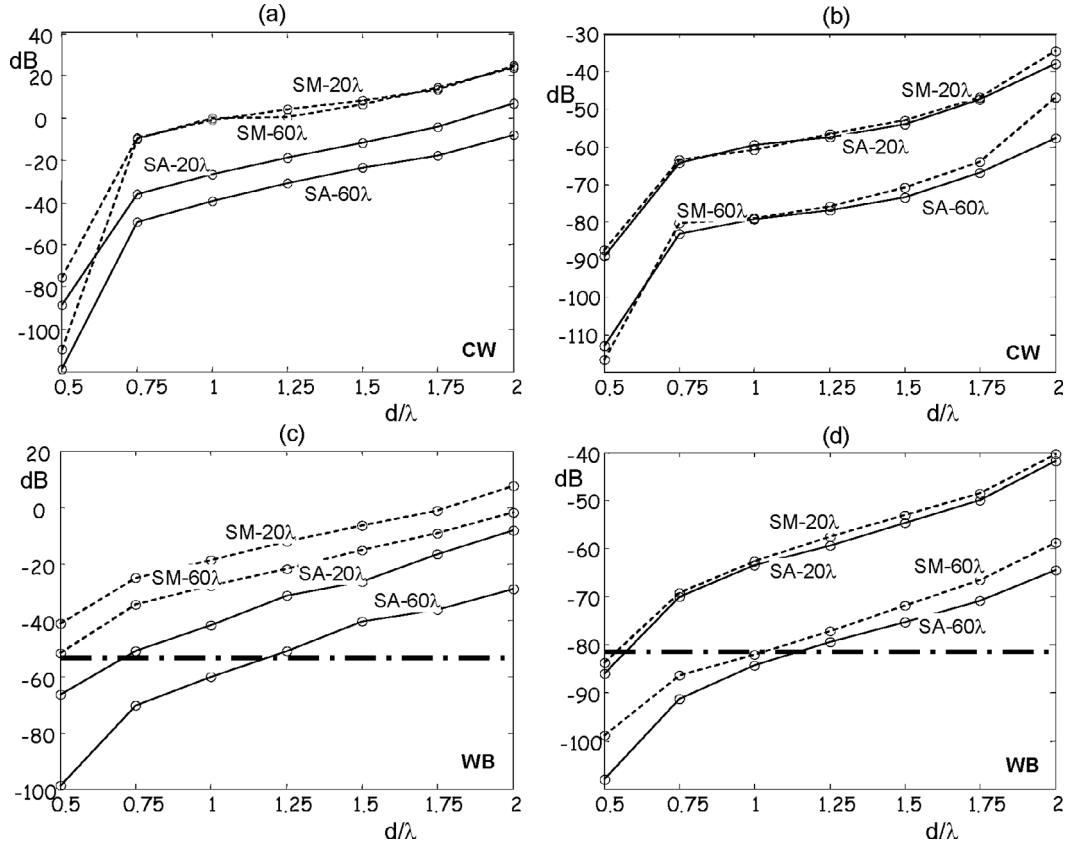

Fig. 12. Evolution of SL_{Peak} relative to ML_{Peak} in decibels, (a) and (c) and of SL_{Average} (b) and (d) for a small aperture with $D = 20\ \lambda$ and a large aperture with $D = 60\ \lambda$, as a function of the normalized interelement distance d/λ. Simulations have been made for the arrays in pulse-echo focusing at $R^F = D^2/8\ \lambda$, $\phi^F = 0°$, $\theta^F = 30°$. In these graphics, the wavelength λ is fixed to 0.5 mm, and the distance between elements d is varied from 0.5 λ to 2 λ. The element size is $e = 0.8$ d. Above, CW excitation. Below, WB pulse.

using the SA array as phased array, there is a limit on the elements' size in order to avoid zeros on the main beam; a limit of $e = 1.25\ \lambda$, which produce zeroes at $|\theta| = 56°$, can be reasonable.

VI. Conclusions

The capability of SA arrays for 3-D beamforming has been theoretically analyzed and compared with the equivalent SM array. Assuming that the main-lobe properties of equivalent SM and SA arrays are similar, we have centered the analysis on the side-lobe region.

In order to facilitate the analysis, this paper uses an approach that allows evaluating the grating lobes of a SA array by three factors: the periodicity factor P, the bandwidth factor F_{WB}, and the element factor H_e. We have shown that P has an inverse dependence on the number of elements of the SA array, F_{WB} depends inversely to the square root of the number of elements and to the pulse relative bandwidth, and H_e depends on the element size, given that the sector-like shape of the elements and their orientation is not very important when the elements are rather small.

Using point-like elements (FA approach in Section III and wide band pulses in Section IV), the effect of the geometrical distribution of elements in the aperture has been enhanced. In this sense, we have shown that rotating the array rings or changing the rate d/λ have a small effect on the peak of the side-lobe region (SL_{Peak}). However, there is an inverse dependence of this parameter with respect to the number of array elements. In wide band, where only a part of the elements simultaneously contribute to grating-lobe formation, the cancellation of grating lobes is reduced and, therefore, the periodicity factor is increased. Related to the mean value of the side-lobe region, we have shown that SL_{Average} has small dependence on the array type (equivalent SM and SA arrays have similar SL_{Average} values) or on the interelement distance (d/λ), presenting however a greater dependence on the number of elements.

The effect of the elements' real size also has been described in detail in Section V. We have shown that the lateral response of a SA array is modulated by the element factor H_e which, for small elements, can be approximated to the response of the equivalent squared transducer in its main directions. This approximation facilitates the steered-beam analysis of SA arrays and the array design.

From the analysis, we conclude that it is possible to design SA arrays with interelement distance and element size beyond $\lambda/2$ (e.g., $d = 1.2\lambda$, $e = \lambda$) with beam characteristics that are perfectly valid for volumetric imaging applications. In consequence, SA arrays have the advantage of reducing the number of elements and of enlarging

the element size, implying an increase in the SNR associated with the element impedance and with the array active area. However, there is a limit on the elements' size ($e < 1.25\ \lambda$), as we need avoiding the zeros of the element factor H_e for large steering angles.

In contrast, the irregular geometry of SA arrays implies a drawback for their fabrication from piezocomposite techniques [27], especially with small elements (e.g., $e \leq 0.5$ mm). However, capacitive micromachined ultrasonic transducer (CMUT) techniques can be a good solution to this problem, as using a cell resolution of 40 μm, array elements with 0.2 mm of size can be well designed.

References

[1] D. H. Turnbull and F. S. Foster, "Beam steering with pulsed two-dimensional transducer array," *IEEE Trans. Ultrason., Ferroelect., Freq. Contr.*, vol. 38, no. 2, pp. 320–333, 1991.

[2] D. H. Turnbull and F. S. Foster, "Simulation of B-scan images from two-dimensional transducer arrays: Part II—Comparison between linear and two-dimensional phased arrays," *Ultrason. Imag.*, vol. 14, no. 4, pp. 334–353, 1992.

[3] R. E. Davidsen, J. A. Jensen, and S. W. Smith, "Two-dimensional random arrays for real time volumetric imaging," *Ultrason. Imag.*, vol. 16, pp. 143–163, 1994.

[4] E. D. Light, R. E. Davidsen, J. O. Fiering, and T. A. Hruschka, "Progress in two-dimensional arrays for real-time volumetric imaging," *Ultrason. Imag.*, vol. 20, pp. 1–15, 1998.

[5] P. K. Weber, R. M. Schmitt, B. D. Tylkowski, and J. Steck, "Optimization of random sparse 2-D transducer arrays for 3-D electronic beam steering and focusing," in *Proc. IEEE Ultrason. Symp.*, 1994, pp. 1503–1506.

[6] S. Holm and B. Elgetun, "Properties of the beampattern of weight-and layout-optimized sparse arrays," *IEEE Trans. Ultrason., Ferroelect., Freq. Contr.*, vol. 44, no. 5, pp. 983–991, 1997.

[7] A. Trucco, "Thinning and weighting of large planar arrays by simulated annealing," *IEEE Trans. Ultrason., Ferroelect., Freq. Contr.*, vol. 46, no. 2, pp. 347–355, 1999.

[8] S. W. Smith, H. G. Pavy, and O. T. Von Ramm, "High speed ultrasound volumetric imaging system—Part I: Transducer design and beam steering," *IEEE Trans. Ultrason., Ferroelect., Freq. Contr.*, vol. 38, no. 2, pp. 101–108, 1991.

[9] G. Lockwood and F. S. Foster, "Optimizing the radiation pattern of sparse periodic two-dimensional arrays," *IEEE Trans. Ultrason., Ferroelect., Freq. Contr.*, vol. 45, no. 2, pp. 338–348, 1996.

[10] S. Brunke and G. Lockwood, "Broad-bandwidth radiation patterns of sparse two-dimensional Vernier arrays," *IEEE Trans. Ultrason., Ferroelect., Freq. Contr.*, vol. 44, no. 5, pp. 1101–1109, 1997.

[11] A. Austeng and S. Holm, "Sparse 2-D arrays for 3-D phased array imaging—Design methods," *IEEE Trans. Ultrason., Ferroelect., Freq. Contr.*, vol. 49, no. 8, pp. 1073–1086, 2002.

[12] J. L. Schwartz and B. D. Steinberg, "Ultrasparse, ultrawideband arrays," *IEEE Trans. Ultrason., Ferroelect., Freq. Contr.*, vol. 45, pp. 376–393, 1998.

[13] T. S. Sumanaweera, J. Schwartz, and D. Napolitano, "A spiral 2D phased array for 3D imaging," in *Proc. IEEE Ultrason. Symp.*, vol. 2, 1999, pp. 1271–1274.

[14] O. Martínez, "Arrays de anillos segmentados para generación de imagen 3D," Ph.D. dissertation, University Politécnica, Madrid, Spain, Sep. 2000. (in Spanish)

[15] M. Akhnak, O. Martínez, L. G. Ullate, and F. Montero de Espinosa, "64 elements two-dimensional piezoelectric array for 3-D imaging," *Ultrasonics*, vol. 40, pp. 139–143, 2002.

[16] P. R. Stepanishen, "Transient radiation from pistons in an infinite planar baffle," *J. Acoust. Soc. Amer.*, vol. 49, no. 5-2, pp. 1629–1639, 1971.

[17] A. Reilly and G. Hayward, "A model to predict the transient radiation from segmented annular apertures radiating into solid media," *IEEE Trans. Ultrason., Ferroelect., Freq. Contr.*, vol. 43, no. 2, pp. 263–269, 1996.

[18] O. Martínez, L. G. Ullate, and F. Montero, "Computation of the ultrasonic field radiated by segmented-annular arrays," *J. Comput. Acoust.*, vol. 9, no. 3, pp. 757–772, 2001.

[19] S. J. Norton, "Annular array imaging with full aperture resolution," *J. Acoust. Soc. Amer.*, vol. 92, no. 6, pp. 3202–3206, 1992.

[20] L. G. Ullate, O. Martínez, M. Parrilla, and M. A. G. Izquierdo, "3D beamforming with ultrasonic divided-ring arrays," *Ultrasonics*, vol. 40, pp. 123–127, 2002.

[21] O. Martínez, L. Gómez-Ullate, and A. Ibáñez, "Comparison of CW beam patterns from segmented annular arrays and squared arrays," *Sens. Actuators*, vol. 85, no. 1-3, pp. 33–37, 2000.

[22] Y. Mendelsohn and E. Wiener-Avnear, "Simulations of circular 2D phase-array ultrasonic imaging transducers," *Ultrasonics*, vol. 39, pp. 657–666, 2002.

[23] J. J. Giesey, P. L. Carlson, D. W. Fitting, and C. R. Meyer, "Speckle reduction in pulse-echo ultrasonic imaging using a two-dimensional receiving array," *IEEE Trans. Ultrason., Ferroelect., Freq. Contr.*, vol. 39, no. 2, pp. 167–173, 1992.

[24] T. Fjield and K. Hynynen, "The combined concentric ring and sector-vortex phased array for MRI guided ultrasound surgery," *IEEE Trans. Ultrason., Ferroelect., Freq. Contr.*, vol. 44, no. 5, pp. 1157–1167, 1997.

[25] Y. Wang and M. O'Donnell, "Compounding of a forward-viewing ring-annular ultrasound array system," *Ultrason. Imag.*, vol. 23, pp. 147–160, 2001.

[26] H. P. Schwarz, "Development of a divided ring array for three-dimensional beam steering in ultrasonic non-destructive testing," in *Proc. IEEE Ultrason. Symp.*, 1987, pp. 859–861.

[27] O. Martínez, M. Akhnak, L. G. Ullate, and F. Montero, "A small 2D ultrasonic array for NDT applications," *NDT&E Int.*, vol. 36, pp. 57–63, 2003.

[28] C. A. Balanis, *Antenna Theory, analysis and design.* New York: Wiley, 1982, pp. 206–213.

[29] B. Piwakowski and S. Khalid, "A new approach to calculate the field radiated from arbitrarily structured transducer arrays," *IEEE Trans. Ultrason., Ferroelect., Freq. Contr.*, vol. 46, no. 2, pp. 422–440, 1999.

[30] G. Godoy, "Metodología de diseño de arrays bidimensionales de geometría anular para generación de imagen ultrasónica 3D," Ph.D. dissertation, Universidad Nacional de Educacion a Distancia (UNED), Madrid, Spain, 2004. (in Spanish)

[31] B. D. Steinberg, *Principles of Aperture and Array System: Including Random and Adaptive Arrays.* New York: Wiley, 1976.

[32] S. J. Norton, "Theory of acoustic imaging," Ph.D. dissertation, Stanford University, Technical Report 4956-2, 1976, pp. 72–7 3.